Atmospheric
Measurement
Techniques
Discussions

Open Access

Atmospheric aerosol characterization with a ground-based SPEX spectropolarimetric instrument

G. van Harten[1], J. de Boer[1], J. H. H. Rietjens[2], A. Di Noia[2], F. Snik[1], H. Volten[3], J. M. Smit[2], O. P. Hasekamp[2], J. S. Henzing[4], and C. U. Keller[1]

[1]Leiden Observatory, Leiden University, Leiden, the Netherlands
[2]SRON Netherlands Institute for Space Research, Utrecht, the Netherlands
[3]Centre for Environmental Quality, National Institute for Public Health and the Environment (RIVM), Bilthoven, the Netherlands
[4]Netherlands Institute for Applied Scientific Research – TNO, Utrecht, the Netherlands

Correspondence to: G. van Harten (harten@strw.leidenuniv.nl)

Discussion Paper | Discussion Paper | Discussion Paper | Discussion Paper |

AMTD

7, 5741–5768, 2014

Aerosol polarimetry

G. van Harten et al.

Title Page

Abstract	Introduction
Conclusions	References
Tables	Figures

|◀ ▶|

◀ ▶

Back Close

Full Screen / Esc

Printer-friendly Version

Interactive Discussion

Abstract

Characterization of atmospheric aerosols is important for understanding their impact on health and climate. A wealth of aerosol parameters can be retrieved from multi-angle, multi-wavelength radiance and polarization measurements of the clear sky. We developed a ground-based SPEX instrument (groundSPEX) for accurate spectropolarimetry, based on the passive, robust, athermal and snapshot spectral polarization modulation technique, and hence ideal for field deployment. It samples the scattering phase function in the principal plane in an automated fashion, using a motorized pan/tilt unit and automatic exposure time detection. Extensive radiometric and polarimetric calibrations were performed, yielding values for both random noise and systematic uncertainties. The absolute polarimetric accuracy at low degrees of polarization is established to be $\sim 5 \times 10^{-3}$. About 70 measurement sequences have been performed throughout four clear-sky days at Cabauw, the Netherlands. Several aerosol parameters were retrieved: aerosol optical thickness, effective radius, and complex refractive index for fine and coarse mode. The results are in good agreement with the co-located AERONET products, with a correlation coefficient of $\rho = 0.932$ for the total aerosol optical thickness at 550 nm.

1 Introduction

Atmospheric aerosols, also known as particulate matter, are particles or droplets suspended in the air. Some types are naturally occurring, such as pollen, spores, sea salt, desert dust and volcanic ash, others are mostly anthropogenic, such as sulfates, nitrates, soot, smoke and ashes from combustion or forest fires, or ammonia salts from agriculture.

Studying aerosols and their spatial and temporal distribution is of great importance because of their impact on health and climate. Exposure to fine particulate air pollution triggers asthma attacks, can lead to lung diseases, and is associated with

Title Page

Abstract | Introduction

Conclusions | References

Tables | Figures

|◄ | ►|

◄ | ►

Back | Close

Full Screen / Esc

Printer-friendly Version

Interactive Discussion

natural-cause mortality (Beelen et al., 2014). Health effects are usually worse for smaller particles, because they can penetrate deeper into the lungs. Since anthropogenic aerosols are generally smaller than their natural counterparts, air-polluted areas are not only dangerous because of the larger amount of particles. The toxicity is also dependent on the particles' shape (sharpness, surface area) and chemical composition.

The influence of aerosols on the climate by means of radiative forcing is still very uncertain (IPCC, 2013). Forcing mechanisms include the direct and indirect aerosol effect. The direct effect is the scattering or absorption of sunlight by aerosols, which overall has a strong cooling effect. However, particular aerosols like black carbon can make a positive radiative forcing. The indirect aerosol effect means that aerosols, being cloud condensation nuclei, stimulate the formation of clouds, which scatter incoming sunlight back into space. Moreover, the droplets in these clouds tend to be smaller, resulting in an even higher albedo and less efficient precipitation, which implies longer life times. The lack of knowledge about atmospheric aerosol load, properties, and their interaction with clouds, makes the input for and verification of climate models and atmospheric chemistry transport models uncertain.

Atmospheric aerosol measurements from the ground are either performed in-situ or as remote sensing. The most prevalent in-situ measurement method is:

– *Particulate matter (PM) monitoring.* Air is sucked through sampling heads that let particles pass which have a diameter smaller than e.g. 10 or 2.5 µm (referred to as PM_{10} and $PM_{2.5}$, respectively). The accumulated particles are manually weighed (reference method) or quantified using their attenuation of beta radiation (automated method) (e.g. McMurry, 2000). The chemical composition can be determined through lab analysis.

Remote sensing of aerosols often involves the following techniques:

– *Lidar.* A laser pulse is sent into the atmosphere, after which the arrival times and intensities of the backscatter are measured. This results in altitude profiles of the

Aerosol polarimetry

G. van Harten et al.

Title Page

Abstract	Introduction
Conclusions	References
Tables	Figures

◀◀   ▶▶

◀   ▶

Back   Close

Full Screen / Esc

Printer-friendly Version

Interactive Discussion

aerosol extinction coefficient. The employment of multiple wavelengths provides the Ångström exponent, an indicator for particle size. An optional depolarization measurement provides information on the aerosol type (e.g. Murayama et al., 1999).

- *Direct sun measurements.* The extinction of the direct solar beam is measured, and translated into an aerosol optical thickness (AOT). The wavelength dependence of the AOT is an indicator for particle size distribution (O'Neill et al., 2003). Regular instrument calibrations on high mountains provide the top-of-atmosphere irradiance (Holben et al., 1998).

- *Diffuse sky measurements.* Sunlight scattered in the atmosphere is measured at multiple angles and wavelengths, and compared with radiative transfer calculations in model atmospheres. A variety of aerosol parameters can be retrieved, e.g. optical thickness, size distribution and complex refractive index, indicative of chemical composition (e.g. Dubovik and King, 2000). The added value of polarization measurements has been shown for satellite geometry by Mishchenko and Travis (1997); Mishchenko et al. (2004); Hasekamp and Landgraf (2007), and for ground-based geometry by Boesche et al. (2006); Li et al. (2009). The advantage of using this method is that it provides fast and cost-effective measurements of various important aerosol parameters for climate and health studies, that may be related directly to both other ground-based measurements as well as aerosol optical thickness retrieved from satellite data.

With our groundSPEX instrument, we aim at performing multi-angle multi-wavelength diffuse sky radiometry and polarimetry with sub-percent absolute polarimetric accuracy. We describe the instrument design and calibration, including the radiometric and polarimetric performance. We present clear-sky measurements and the retrieved aerosol parameters, and compare those to the co-located AERONET products.

2 Measurements

2.1 GroundSPEX instrument

The measurements are performed with a dedicated ground-based version of the SPEX instrument for satellite-based atmospheric aerosol characterization (van Harten et al., 2011). This instrument measures the spectral radiance and linear polarization of sky-light using spectral polarization modulation. In this technique, a carefully selected combination of birefringent crystals with a total retardance of δ encodes the degree (P_L) and angle (ϕ_L) of linear polarization as the amplitude and phase (ψ) of a carrier wave in the intensity spectrum I_0 (see Fig. 1), according to (Snik et al., 2009):

$$S_{\pm}(\lambda) = \frac{1}{2}I_0(\lambda)[1 \pm P_L(\lambda)\cos(\psi(\lambda))], \tag{1a}$$

$$\psi(\lambda) \equiv \frac{2\pi\delta(\lambda)}{\lambda} + 2\phi_L(\lambda). \tag{1b}$$

This modulation technique enables snapshot polarimetry at high accuracy, using a robust instrument with no moving parts, ideal for field deployment.

The spectral carrier wave is created using the following static train of optics:

– *Achromatic quarter-wave retarder with fast axis at 0° (horizontal).* Incoming linear polarization at 45° is converted into circular polarization, and vice versa. In this way, the instrument is turned into a full linear polarimeter, while becoming insensitive to circular polarization. An off-the-shelf N-BK7 Fresnel rhomb from Thorlabs is used, with a maximum retardance deviation of 2 % across the visible wavelength range. Calibration of misalignment and retardance deviation is described in Sect. 2.2.4.

– *Multiple-order retarder with fast axis at 45°.* The ellipticity of the incoming polarization is modulated in a strongly wavelength dependent way using birefringent crystals. A subtractive combination of 1.63 mm quartz and 3.83 mm magnesium

fluoride creates ~ 43 modulation periods within 400–900 nm, with the size of a period ranging from ~ 5–25 nm from the blue to the red end, respectively. For this crystal combination, manufactured by B. Halle, the thermal dependence of the retardance of the individual crystals largely cancels out: for a temperature range of ±20 K the measurement of the angle of linear polarization is stabilized to within ±1.5°. Section 2.2.4 shows that this has a negligible impact on the degree of linear polarization, our main observable.

– *Polarizing beam-splitter, splitting linear polarization at 0 and 90°.* This analyzer turns the ellipticity modulation into a sinusoidal spectral intensity modulation, according to Eq. (1a). Each beam out of the polarizing beam-splitter carries the full linear polarization information, but their modulations are exactly out of phase (see Fig. 1). In this way, the sum of the two beams yields the unmodulated intensity spectrum I_0 at full resolution. The redundancy in the both spectrally and spatially modulated polarization is used for a post-facto differential transmission correction (van Harten et al., 2014b). This correction typically decreases the associated error in the degree of linear polarization by an order of magnitude. Moreover, this quasi beam-exchange technique strongly reduces the polarimetric errors due to uncorrected dark signal. The polarizing beam-splitter is a calcite Foster prism from Melles Griot, with an extinction ratio of 10^{-5}.

The two beams out of the polarizing beam-splitter are focussed onto 550 μm fibers by 35 mm focal length lenses, yielding a field-of-view of 0.9°, with an entrance aperture of 1 cm^2. The fibers are fed into two synchronized spectrographs from Avantes, both equipped with a 3648 pixels, 16 bits CCD detector, 600 lines mm^{-1} reflection grating, and a 25 μm entrance slit, resulting in a wavelength range of 360–910 nm at 0.8 nm resolution, using an order-sorting filter. The optics and spectrographs are positioned in an IP66 weatherproof camera housing from 2B Security, together with the laptop that is controlling the spectrograph and motorized pan/tilt mount. The laptop can connect to a computer network using LAN or WiFi, after which a remote desktop connection can

be established to control the instrument from anywhere. A fused silica entrance window behind a 15 cm long entrance tube protects the optics and electronics from rain, and provides straylight baffling. The IP66 pan/tilt mount from 2B Security rotates at a speed of $50° \, s^{-1}$ in the azimuth and $20° \, s^{-1}$ in the altitude direction, with electronic position accuracies of $0.01°$ and $0.006°$, respectively.

The instrument control software is able to autonomously execute a measurement sequence upon receiving a user-supplied list with pan and tilt angles. Per pointing, the spectrograph first records a trial spectrum at a very short exposure time (10 ms), that is subsequently extrapolated to determine the exposure time for a desired intensity value. Typical exposure times are 50–200 ms, and 50 spectra are averaged for a signal to noise ratio of > 370 per pixel to enable spectral line polarimetry with a sensitivity of at least 2.7×10^{-3}, so the measurement cadence is about 10 s. Note that this paper does not deal with line polarimetry, but with continuum polarimetry in 10 nm wide bands, resulting in a polarimetric noise of only 10^{-4}.

2.2 Calibrations

Several calibrations need to be performed before the data can be fed into the aerosol retrieval algorithm. Moreover, a careful quantification of the measurement errors and their statistics is crucial to obtain reliable error bars on the retrieved aerosol parameters.

2.2.1 Wavelength calibration

The wavelength calibration of the spectrographs is performed using a mercury/argon line lamp, fiber-connected to the spectrographs. Nine spectral lines have been identified across the spectrum, and a third-order polynomial relates each detector pixel to a wavelength. The root-mean-square deviation between the theoretical line wavelengths and the calibrated values is 0.01 nm. The spectra of one spectrograph are matched to the wavelengths of the other spectrograph using linear interpolation.

Title Page

Abstract | Introduction

Conclusions | References

Tables | Figures

⏮ | ⏭

◀ | ▶

Back | Close

Full Screen / Esc

Printer-friendly Version

Interactive Discussion

2.2.2 Detector dark signal

The instrument is usually exposed to direct sunlight, and the detector is uncooled, so a careful dark current subtraction is important. The dark current cannot be measured during a measurement sequence, because the instrument is not equipped with a me-
5 chanical shutter. Therefore, the dark current was characterized offline as a function of exposure time and temperature, using the built-in temperature sensor. A typical detector temperature range during a day is 20–40 °C. It was found that the bias strongly decreases with increasing temperature (from 1000 to 400 analog-to-digital units (ADU)), for shorter exposure times the dark current increases linearly with exposure time, and
10 at a higher rate for higher temperatures, but for exposure times above 100 ms the increase with exposure time gets strongly suppressed, with this non-linearity being worse for higher temperatures. For each pixel, a 4th-degree 2-D polynomial was fitted to the dark calibration measurements, providing a continuous correction model (see Fig. 2).

    The root-mean-square deviation between the model and the calibration measure-
15 ments is 9 ADU for each pixel. Although these residuals are centered around zero, it is not random noise; it shows dependencies on temperature and exposure time. This is presumably a side-effect of the calibration method: the exposure time was repeatedly increased from 1 to 1000 ms, while the temperature was varied between 10 and 45 °C in a non-linear way. There may have been a lag between the temperature at the detec-
20 tor and the thermometer, particularly at fast temperature changes. After calibration, the effect of temperature gradients is counteracted with the use of optical black detector pixels. The average value of those 13 pixels at the time of measurement, compared to their average value at the time of calibration, is added to the dark model as a dynamic correction. Pixel-to-pixel variations of the dark current calibration residuals seem
25 random, with a standard deviation of 6 ADU.

Title Page

Abstract | Introduction

Conclusions | References

Tables | Figures

|◄ | ►|

◄ | ►

Back | Close

Full Screen / Esc

Printer-friendly Version

Interactive Discussion

2.2.3 Differential transmission

The next calibration step is a correction for the differential transmission for the two optical paths. Alignment differences lead to a slowly spectrally varying differential transmission of 0.8–1.2, an issue with the order-sorting filter in one of the spectrographs creates transmission spikes of ±10 % at 603 and 622 nm, and differences in the detector chips cause a differential spectral fringe pattern with an amplitude of 5 %. It is important to note that a flatfield spectrum needs to be measured with strictly unpolarized light; in case of polarization, the corresponding modulation pattern will be introduced into every single measurement during flatfielding, thereby creating spurious polarization. Light sources are typically polarized at the ~ 5 % level, therefore an unpolarized sky spectrum was used as flatfield. To that end, the polarization of skylight was measured throughout the principal plane in steps of 1°, and the least polarized spectrum ($P_{\mathrm{L}} < 10^{-3}$) has been selected. Residual differential transmission is dynamically corrected for by the demodulation algorithm as described by van Harten et al. (2014b). They show that the eventual error in the degree of linear polarization due to differential transmission is smaller than 10^{-4}.

2.2.4 Polarimetric calibration

Calibration of the polarization measurements is performed by inserting a rotatable polarizer in the entrance tube of the instrument. The thus measured spectral polarization describes the spectral efficiency ϵ of the polarimetry, which is ~ 0.95 for wavelengths longer than 600 nm. At shorter wavelengths the efficiency gradually decreases to ~ 0.85 at 400 nm, because the contrast of the faster modulation gets washed out by the spectrograph slit function. The efficiency not only depends on the wavelength, but also on the angle of linear polarization of the incident light. In case the quarter-wave retarder is not exactly a quarter-wave, polarization at 45° will partly leak through the multiple-order retarder without being modulated. The maximum spectral retardance deviation of 2 % for the Fresnel rhomb leads to a decrease in modulation amplitude

Title Page

Abstract | Introduction

Conclusions | References

Tables | Figures

|◄ | ►|

◄ | ►

Back | Close

Full Screen / Esc

Printer-friendly Version

Interactive Discussion

of 5×10^{-4}, which is barely measurable. Misalignments of the quarter-wave retarder and multiple-order retarder decrease the modulation amplitudes for both polarization at 0 and 45°, but not by the same amount. For example, realistic misalignments of ±2° cause a differential modulation efficiency of 2 %. Therefore, the polarization calibration measurements are performed for polarizer orientations of $0, 10, \ldots, 170°$. Based on the angle of linear polarization of a sky measurement, the corresponding spectral efficiency is constructed by interpolation of the calibration measurements.

The uncertainty in the polarization measurements is composed of systematic uncertainty and random noise. Potential sources of systematic uncertainties are imperfect dark signal subtraction and instrument changes with temperature. Using the equations in van Harten et al. (2014b) for the propagation of uncorrected dark current, for typical intensities in the three spectral bands as shown in Fig. 1, the relative polarimetric uncertainties due to dark signal are 0.1, 0.2 and 2.3 % at 441, 675 and 870 nm, respectively. Note that the calibration measurement for the polarimetric efficiency is also affected by the same amount. The athermal multiple-order retarder yields a thermal stability in the angle of linear polarization of ±1.5° over a ±20 K temperature range. The corresponding uncertainty in the degree of linear polarization, through the dependency of the polarimetric efficiency correction on the angle of linear polarization, is negligible. Spectrograph defocus due to temperature changes leads to a loss of spectral resolution, thereby directly impacting the modulation contrast, just like the spectrograph slit function. A typical spot degradation of 1 pixel per 20 K for an $f/4$ aluminum spectrograph results in a reduction of the modulation amplitude of 2 % in the blue, where the modulation period is ∼ 6 nm, whereas in the red the efficiency decreases by only 0.1 % because the modulation period is 4 times larger. The vast majority of the measurements were taken within 5 K of the efficiency calibration measurements, leading to thermal uncertainties in the polarimetric efficiency of 0.5, 0.1 and 0.03 % at 441, 675 and 870 nm, respectively. The total root-sum-squared relative systematic polarimetric uncertainties at the aforementioned wavelengths are 0.5, 0.3 and 3.2 %, respectively. In the blue the polarization error is dominated by thermal spectrograph defocus, whereas

in the red the main error source is residual dark signal. A complete error analysis for spectrally modulated polarization measurements, including measurements of the temperature sensitivity of the polarization, will be presented in forthcoming papers (van Harten et al., 2014a; Rietjens et al., 2014).

The random noise in the polarization is determined by fitting each polarization curve as a function of scattering angle θ for tens of principal plane scans to an empirical function by Dahlberg (2010), given by:

$$P_L(\theta) = \frac{\sin^2(\beta_1\theta + \beta_2)}{1 + \cos^2(\beta_1\theta + \beta_2) + 2\beta_3/(1 - \beta_3)}. \tag{2}$$

The free parameters β_1 and β_2 allow for a possible pointing error, as well as a shift of the maximum polarization to a scattering angle different than 90°, which is often observed (e.g. Boesche et al., 2006). The atmospheric depolarization factor β_3 determines the maximum degree of linear polarization. The best fit values for β are not used, but they are needed to leave no systematic fit residuals in order to get a reliable value for the random noise in the degree of linear polarization. The root-mean-square of the residuals of all fits together quantifies the absolute random polarimetric noise, which is 0.004, 0.006 and 0.006 at 441, 675 and 870 nm, respectively. These values are an order of magnitude larger than photon noise and random instrumental errors like detector readout noise and pointing instability, so it is believed to be dominated by sky variations like very thin inhomogeneously distributed cirrus that is not visible to the naked eye.

As an independent verification of the polarimetric calibration, the polarization at 870 nm of the aforementioned principal plane scans is compared with the co-located AERONET CIMEL sun photometer, equipped with polarization filters at different orientations. For 93 % of the data the difference between the instruments is within their combined root-sum-squared error bar, for an uncertainty of 0.01 for the sun photometer (Li et al., 2009). This hints at an overestimation of the groundSPEX error bar, for

Aerosol polarimetry

G. van Harten et al.

example because the particular temperatures and exposure times are associated with a smaller than average residual dark current.

A summary of the polarimetric calibration is given in Table 1.

2.2.5 Radiometric calibration

The radiance measurements are calibrated against the co-located AERONET CIMEL sun photometer, using the same tens of principal plane scans that were used for the polarimetric calibration. The measurements were not strictly synchronized; on average they were performed within 11 min of each other, and within 1.7° scattering angle. However, the stable sky conditions and smooth variation of radiance with time and scattering angle allow us to linearly interpolate the two AERONET scans closest in time to the time of the groundSPEX measurement, followed by a linear interpolation to groundSPEX' scattering angles. For each scan there is a perfect linear relationship between AERONET and groundSPEX, but the gain $\gamma(\lambda)$ that relates groundSPEX radiances in $ADU\,ms^{-1}$ to CIMEL radiances in $\mu W\,cm^{-2}\,sr^{-1}\,nm^{-1}$ changes significantly from scan to scan. The origin of this phenomena is unknown, it is not correlated with time or temperature, and it can not be explained by residual dark signal or scattering angle dependent straylight. Therefore, the standard deviation of all the best fit values for γ translates into a relative systematic intensity uncertainty of 2.8, 4.5 and 5.7 % at 441, 675 and 870 nm, respectively. The standard deviation of the residuals for all these fits combined gives the relative random intensity noise of 2.6, 4.6 and 7.6 %, respectively. The gain itself is found by fitting the data of all scans together, yielding values for $\gamma(\lambda)$ of 0.0429, 0.0229 and 0.1107, respectively. The deviations between the instruments clearly scale with intensity, therefore a weighted least squares fit is applied, where the weights are given by the inverse radiances squared. The result of the radiometric calibration is shown in Fig. 3, where the dashed lines represent the total root-sum-squared systematic and random error.

A summary of the radiometric calibration is given in Table 1.

Title Page

Abstract | Introduction

Conclusions | References

Tables | Figures

◄ | ►

◄ | ►

Back | Close

Full Screen / Esc

Printer-friendly Version

Interactive Discussion

2.2.6 Pointing calibration

The absolute pointing is calibrated by putting the sun at the center of the field-of-view at different times during the day, after inserting a neutral density filter to avoid overexposure. The standard deviation of the hence obtained absolute pan and tilt angles is 0.2°,
5 yielding a total pointing accuracy of 0.3°. The electronic pointing errors are negligible compared to this calibration accuracy.

2.3 Observations

Several atmospheric scattering measurements were performed with the groundSPEX instrument at the Cabauw Experimental Site for Atmospheric Research (CESAR Ob-
10 servatory) in the Netherlands (51.971° N, 4.927° E), also known as Cabauw (http://www.cesar-observatory.nl). This site, located in a rural environment with mainly grassland within a radius of 10 km, but in between extended urban areas, hosts a large variety of instrumentation, e.g. for research of the atmospheric boundary layer, clouds, aerosols, greenhouse gases, the Baseline Surface Radiation Network (BSRN), and
15 the AErosol RObotic NETwork (AERONET) (Apituley et al., 2008; Holben et al., 1998).
Throughout four mostly cloudless days in 2013, viz. 7, 8 and 9 July, and 5 September, the instrument sampled the intensity and polarization at 360–910 nm in the principal plane, defined by the instrument, zenith and the sun. Each principal plane scan consisted of 8 to 25 viewing zenith angles between 60 and −60°. Angles closer to the
20 horizon were avoided because the plane-parallel model atmosphere in the aerosol retrieval algorithm is not valid at larger zenith angles, and the contribution of the limitedly known albedo increases close to the horizon, as well as the variability of the scene. The groundSPEX instrument cannot measure within 6° from the sun, because of straylight and overexposure.
25 Cloud-screening has been performed using the co-located total sky imager (TSI) that records an image of the entire sky every minute. Since the sky was clear for most of the time, any changes because of clouds drifting in or cirrus appearing were clearly visible.

Principal plane scans were only considered acceptable if the entire principal plane is clear during the entire scan. The daily average relative humidities were $\sim 70\%$.

3   Aerosol retrieval

The atmospheric aerosol properties are retrieved from the scattered radiance and degree of linear polarization at 441, 675 and 870 nm, using the inversion algorithm described by Di Noia et al. (2014). This algorithm performs an iterative retrieval of a set of aerosol parameters (aerosol column concentration, effective radius, and complex refractive index for fine and coarse mode) along with the surface albedo, using Phillips–Tikhonov regularization. The forward model is described by Hasekamp and Landgraf (2005). The initial guess is provided by a neural network, trained using representative simulated data (Di Noia et al., 2014). The distinction between systematic and random errors in the radiance and polarization measurements (see Sect. 2.2) allows us to assess the impact of measurement errors on retrieved aerosol parameters. We showed in Sect. 2 that systematic polarization errors are caused by bias drift and temperature, resulting in an increase or decrease in the degree of linear polarization for all wavelengths at the same time. The systematic uncertainty in the radiances also has the same sign for all wavelengths, but is not related to the sign of the polarization error. Therefore, the propagation of systematic errors has been calculated by performing the aerosol retrieval for 9 scenarios: radiance without systematic error, radiance minus systematic error, and radiance plus systematic error, all in combination with polarization without and with positive and negative systematic error. The propagation of random errors is captured in the retrieval error covariance matrix, which is calculated as part of the iterative inversion process. The size of the random measurement errors is similar to (radiometry) or smaller than (polarimetry) the systematic uncertainty. Moreover, ~ 100 data points are fitted during the retrieval for one principal plane measurement (radiance and polarization at 3 wavelengths at ~ 15 scattering angles, see Fig. 4), so the random errors will average out by a factor of $\sqrt{100} = 10$, whereas the systematic errors move

Title Page

Abstract | Introduction

Conclusions | References

Tables | Figures

◀◀ | ▶▶

◀ | ▶

Back | Close

Full Screen / Esc

Printer-friendly Version

Interactive Discussion

entire datasets up or down. Therefore, the impact of random errors on the retrieved aerosol parameters is assumed to be negligible compared to systematic uncertainties.

4   Results

The measured spectral radiance and degree of linear polarization as a function of scat-
tering angle for one principal plane scan is shown in Fig. 4, together with the retrieval
algorithm best fit. The error bars represent the total uncertainty in the measurements,
viz. the root-sum-squared systematic and random errors. The fit has a reduced chi-
squared of 0.57, and yields an aerosol optical thickness (AOT) at 550 nm of $0.228^{+0.013}_{-0.018}$
(see Fig. 5).

9 July shows both the lowest and highest AOT of our dataset, as well as the steep-
est AOT change in time. Therefore, the AOT time series of 9 July is shown in Fig. 5,
together with the AERONET direct sun AOT, calculated using the Beer–Lambert–
Bouguer law (Holben et al., 1998). The error bars on the groundSPEX measurements
represent the systematic errors as the lowest and highest retrieved AOT for the 9 input
scenarios as described in Sect. 3. The AERONET level 1.5 data are cloud-screened
and calibrated, but post-calibration has not been applied, hence the AOT error bar of
±0.02 (Eck et al., 1999). The ability of groundSPEX to accurately measure AOT, often
considered the main aerosol parameter, is clear, even in the rapidly changing atmo-
spheric conditions around 10:00 UTC, even without directly observing the sun.

A comparison between groundSPEX and AERONET of retrieved aerosol parameters
for the entire dataset is shown in Fig. 6. The AERONET AOT in the upper plot is the
total AOT retrieved from direct sun measurements at multiple wavelengths, interpolated
to 550 nm (so that includes the data from Fig. 5). A least squares fit yields a regression
line of groundSPEX = 0.005 + 0.893 AERONET, with a Pearson correlation coefficient
of $\rho = 0.932$.

The AOT of the fine and coarse mode measured with AERONET are retrieved
using the Spectral Deconvolution Algorithm (SDA) (O'Neill et al., 2001, 2003), that

Aerosol polarimetry

G. van Harten et al.

Title Page

Abstract	Introduction
Conclusions	References
Tables	Figures

|◀ | ▶|

◀ | ▶

Back | Close

Full Screen / Esc

Printer-friendly Version

Interactive Discussion

employs the spectral shape of the direct sun AOT. These AOT retrievals are performed at 500 nm, resulting in a slight overestimation of ~ 0.01 compared to groundSPEX at 550 nm. The error bars on the SDA fine and coarse mode AOT are provided with the retrieval results of AERONET.

The effective radius of the fine and coarse mode, as well as the spectrally averaged total complex refractive index as determined by AERONET, are retrieved with the inversion algorithm by Dubovik and King (2000) that accounts for non-spherical particles (Dubovik et al., 2006), using both direct sun and diffuse sky measurements. The errors in the effective radii are unknown. The errors in the total refractive index are 0.04 for the real part and 50 % for the imaginary part (Dubovik et al., 2000). For ground-SPEX, the total refractive index is the AOT-weighted sum of the retrieved spectrally flat fine and coarse mode refractive indices.

All error bars shown for groundSPEX are the result of systematic measurement uncertainties, for reasons explained in Sect. 3. Only retrievals with a reduced chi-squared smaller than 10 are presented. The absolute chi-squared values do not translate directly into a probability that the data matches the model, due to systematic errors in the data and the model, however, the relative values can still be used as a measure for goodness of fit. To get a feel for the meaning of the absolute and relative chi-squared values, the results in Fig. 6 are color coded based on the chi-squared of the retrievals. For a fair comparison between the different parameters, the plotted range for each aerosol parameter is the total range of possible values.

5 Discussion

It is important to make a clear distinction between the AERONET direct sun total AOT, and the other AERONET products. The AERONET measurement of direct sun AOT is straightforward and reliable, and it is therefore crucial that the groundSPEX total AOT does not differ significantly. Any other AERONET products involve inverse modelling, so there is no absolute ground truth. Moreover, both the data and the error bars, as well as

the inversion algorithms are different for both instruments. The AERONET products are derived from radiance measurements, whereas groundSPEX employs both radiometry and accurate polarimetry. This makes it difficult to interpret discrepancies, so we will limit ourselves here to a qualitative comparison. Applying the groundSPEX aerosol retrieval algorithm to AERONET data would be an interesting future project, to start disentangling the effects of instrument and data reduction (Pust et al., 2011).

Overall there is a very good agreement between groundSPEX and AERONET for all parameters. In particular, the important and widely measured parameter of total AOT matches the AERONET direct sun measurement over a large range of values, and exhibits relatively small error bars compared to the other aerosol parameters. This results in a correlation coefficient of $\rho = 0.932$, even though groundSPEX is not able to measure within 6° of the sun. The measured range of coarse mode AOT and effective radii is quite limited, so future observations under various atmospheric conditions are needed. The measurements of complex refractive index, that is an indicator of chemical composition, are consistent with AERONET, albeit with slightly larger error bars.

6 Conclusions and outlook

We have developed the groundSPEX instrument, an automated sky-scanning spectropolarimeter. An extensive error analysis has been performed, resulting in random and systematic error bars for radiometry and polarimetry. About 70 measurement sequences of the clear sky have been performed throughout four days in 2013 at the CESAR Observatory in the Netherlands. Important aerosol parameters have been retrieved, such as optical thickness, size distribution and complex refractive index. The results are in good agreement with the co-located AERONET products; for instance, the total aerosol optical thickness at 550 nm exhibits a correlation coefficient of $\rho = 0.932$.

The main advantage of groundSPEX compared to AERONET is the measurement of both radiance and linear polarization across the entire visible spectrum (400–900 nm). The passive spectral polarization modulation technique leads to a robust instrument,

Title Page

Abstract | Introduction

Conclusions | References

Tables | Figures

◄ | ►

◄ | ►

Back | Close

Full Screen / Esc

Printer-friendly Version

Interactive Discussion

with a high polarimetric accuracy of $\sim 5 \times 10^{-3}$, at low cost, suitable for deployment in a measurement network. Moreover, the use of diffuse sky measurements and inversions, and the instrument's ability to point in any direction, potentially enables measuring in partially cloudy sky conditions.

GroundSPEX will continue to be employed on a regular basis at the CESAR Observatory as a fast instrument to retrieve optical and microphysical properties of aerosols that are important for climate and health studies. We will build a dataset that will be used to study aerosol parameters in relation to other ground-based measurements as well as satellite measurements. In addition, groundSPEX will provide a valuable and much needed link between ground-based aerosol measurements and data retrieved by satellite instruments, such as GOME-2, MISR, MODIS and OMI, or – hopefully – an airborne or satellite-based version of SPEX itself.

References

Apituley, A., Russchenberg, H., van der Marel, H., Bosveld, F., Boers, R., ten Brink, H., de Leeuw, G., Uijlenhoet, R., Arbresser-Rastburg, B., and Rockmann, T.: Overview of Research and Networking with Ground based Remote Sensing for Atmospheric Profiling at the Cabauw Experimental Site for Atmosspheric Research (CESAR) – the Netherlands, in: Geoscience and Remote Sensing Symposium, 2008, IGARSS 2008, IEEE International, Vol. 3, 903–906, 2008. 5753

Beelen, R., Raaschou-Nielsen, O., Stafoggia, M., et al.: Effects of long-term exposure to air pollution on natural-cause mortality: an analysis of 22 European cohorts within the multicentre ESCAPE project, Lancet, 383, 785–795, 2014. 5743

Boesche, E., Stammes, P., Ruhtz, T., Preusker, R., and Fischer, J.: Effect of aerosol microphysical properties on polarization of skylight: sensitivity study and measurements, Appl. Optics, 45, 8790–8805, 2006. 5744, 5751

Dahlberg, A. R.: All-sky polarization imager deployment at Mauna Loa Observatory, Hawaii, Master's thesis, Montana State University, 2010. 5751

Di Noia, A., Hasekamp, O. P., van Harten, G., Rietjens, J. H. H., Smit, J. M., Snik, F., Henzing, J. S., and Volten, H.: Use of neural networks in ground based aerosol retrievals from multi-angle spectropolarimetric observations, in preparation, 2014. 5754

Dubovik, O. and King, M. D.: A flexible inversion algorithm for retrieval of aerosol optical properties from Sun and sky radiance measurements, J. Geophys. Res., 105, 20673, doi:10.1029/2000JD900282, 2000. 5744, 5756

Dubovik, O., Smirnov, A., Holben, B. N., King, M. D., Kaufman, Y. J., Eck, T. F., and Slutsker, I.: Accuracy assessments of aerosol optical properties retrieved from Aerosol Robotic Network (AERONET) Sun and sky radiance measurements, J. Geophys. Res., 105, 9791–9806, 2000. 5756

Dubovik, O., Sinyuk, A., Lapyonok, T., Holben, B. N., Mishchenko, M., Yang, P., Eck, T. F., Volten, H., Muñoz, O., Veihelmann, B., van der Zande, W. J., Leon, J.-F., Sorokin, M., and Slutsker, I.: Application of spheroid models to account for aerosol particle non-sphericity in remote sensing of desert dust, J. Geophys. Res.-Atmos., 111, D11208, doi:10.1029/2005JD006619, 2006. 5756

Eck, T. F., Holben, B. N., Reid, J. S., Dubovik, O., Smirnov, A., O'Neill, N. T., Slutsker, I., and Kinne, S.: Wavelength dependence of the optical depth of biomass burning, urban, and desert dust aerosols, J. Geophys. Res., 104, 31333, doi:10.1029/1999JD900923, 1999. 5755

Hasekamp, O. P. and Landgraf, J.: Linearization of vector radiative transfer with respect to aerosol properties and its use in satellite remote sensing, J. Geophys. Res., 110, D04203, doi:10.1029/2004JD005260, 2005. 5754

Hasekamp, O. P. and Landgraf, J.: Retrieval of aerosol properties over land surfaces: capabilities of multiple-viewing-angle intensity and polarization measurements, Appl. Optics, 46, 3332–3344, 2007. 5744

Holben, B. N., Eck, T. F., Slutsker, I., Tanré, D., Buis, J. P., Setzer, A., Vermote, E., Reagan, J. A., Kaufman, Y. J., Nakajima, T., Lavenu, F., Jankowiak, I., and Smirnov, A.: AERONET – a

Title Page

Abstract | Introduction

Conclusions | References

Tables | Figures

|◀ | ▶|

◀ | ▶

Back | Close

Full Screen / Esc

Printer-friendly Version

Interactive Discussion

federated instrument network and data archive for aerosol characterization, Remote Sens. Environ., 66, 1–16, 1998. 5744, 5753, 5755

IPCC: Summary for policymakers, in: Climate Change 2013: The Physical Science Basis. Contribution of Working Group I to the Fifth Assessment Report of the Intergovernmental Panel on Climate Change., edited by: Stocker, T. F., Qin, D., Plattner, G.-K., Tignor, M., Allen, S. K., Boschung, J., Nauels, A., Xia, Y., Bex, V., and Midgley, P. M., Cambridge University Press, Cambridge, United Kingdom and New York, NY, USA, 11–12, 2013. 5743

Li, Z., Goloub, P., Dubovik, O., Blarel, L., Zhang, W., Podvin, T., Sinyuk, A., Sorokin, M., Chen, H., Holben, B., Tanré, D., Canini, M., and Buis, J.-P.: Improvements for ground-based remote sensing of atmospheric aerosol properties by additional polarimetric measurements, J. Quant. Spectrosc. Ra., 110, 1954–1961, 2009. 5744, 5751

McMurry, P. H.: A review of atmospheric aerosol measurements, Atmos. Environ., 34, 1959–1999, 2000. 5743

Mishchenko, M. I. and Travis, L. D.: Satellite retrieval of aerosol properties over the ocean using polarization as well as intensity of reflected sunlight, J. Geophys. Res., 102, 16989, doi:10.1029/96JD02425, 1997. 5744

Mishchenko, M. I., Cairns, B., Hansen, J. E., Travis, L. D., Burg, R., Kaufman, Y. J., Vanderlei Martins, J., and Shettle, E. P.: Monitoring of aerosol forcing of climate from space: analysis of measurement requirements, J. Quant. Spectrosc. Ra., 88, 149–161, 2004. 5744

Murayama, T., Okamoto, H., Kaneyasu, N., Kamataki, H., and Miura, K.: Application of lidar depolarization measurement in the atmospheric boundary layer: effects of dust and sea-salt particles, J. Geophys. Res., 104, 31781, doi:10.1029/1999JD900503, 1999. 5744

O'Neill, N. T., Dubovik, O., and Eck, T. F.: Modified Ångström exponent for the characterization of submicrometer aerosols, Appl. Optics, 40, 2368–2375, 2001. 5755

O'Neill, N. T., Eck, T. F., Smirnov, A., Holben, B. N., and Thulasiraman, S.: Spectral discrimination of coarse and fine mode optical depth, J. Geophys. Res., 108, 4559, doi:10.1029/2002JD002975, 2003. 5744, 5755

Pust, N. J., Dahlberg, A. R., Thomas, M. J., and Shaw, J. A.: Comparison of full-sky polarization and radiance observations to radiative transfer simulations which employ AERONET products, Opt. Express, 19, 18602, doi:10.1364/OE.19.018602, 2011. 5757

Rietjens, J. H. H., van Harten, G., Snik, F., Smit, J. M., and Keller, C. U.: Performance of spectrally modulated polarimetry II: data reduction and absolute polarization calibration, in preparation, 2014. 5751

Aerosol polarimetry

G. van Harten et al.

Title Page

Abstract	Introduction
Conclusions	References
Tables	Figures

Back | Close

Full Screen / Esc

Printer-friendly Version

Interactive Discussion

Snik, F., Karalidi, T., and Keller, C. U.: Spectral modulation for full linear polarimetry, Appl. Optics, 48, 1337–1346, 2009. 5745

van Harten, G., Snik, F., Rietjens, J. H. H., Smit, J. M., de Boer, J., Diamantopoulou, R., Hasekamp, O. P., Stam, D. M., Keller, C. U., Laan, E. C., Verlaan, A. L., Vliegenthart, W. A., Ter Horst, R., Navarro, R., Wielinga, K., Hannemann, S., Moon, S. G., and Voors, R.: Prototyping for the Spectropolarimeter for Planetary EXploration (SPEX): calibration and sky measurements, in: Society of Photo-Optical Instrumentation Engineers (SPIE) Conference Series, Vol. 8160, 2011. 5745

van Harten, G., Rietjens, J. H. H., Snik, F., Smit, J. M., and Keller, C. U.: Performance of spectrally modulated polarimetry I: analysis and optimization, in preparation, 2014a. 5751

van Harten, G., Snik, F., Rietjens, J. H. H., Smit, J. M., and Keller, C. U.: Spectral line polarimetry with a channeled polarimeter, in press, 2014b. 5746, 5749, 5750

Title Page

Abstract | Introduction

Conclusions | References

Tables | Figures

|◄ | ►|

◄ | ►

Back | Close

Full Screen / Esc

Printer-friendly Version

Interactive Discussion

Table 1. Summary of the polarimetric and radiometric calibrations.

Measurement	Systematic error			Random error		
λ [nm]	441	675	870	441	675	870
Polarization (P_L)	$0.005\,P_L$	$0.003\,P_L$	$0.032\,P_L$	0.004	0.006	0.006
Radiance (I)	$0.028\,I$	$0.045\,I$	$0.057\,I$	$0.026\,I$	$0.046\,I$	$0.076\,I$
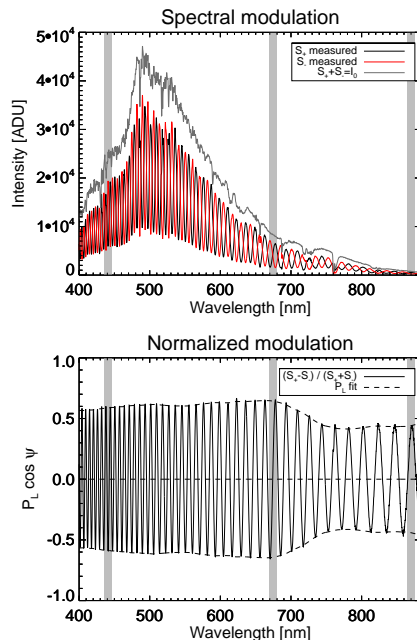
Figure 1. Top. The groundSPEX instrument measures the two perpendicularly modulated spectra S_+ and S_- simultaneously. The degree (P_L) and angle ($\phi_L(\psi)$) of linear polarization are encoded as the relative amplitude and phase of the modulation pattern, respectively. The sum of the two modulated spectra is the intensity spectrum I_0 at full resolution. Bottom. Curve fits of $P_L \cos\psi$ to the normalized modulation in a moving window provide the spectral polarization information. Note the decrease in polarization at 550 nm and above 700 nm, due to the increase in the albedo of grass, called green bump and red edge, respectively. Note also that the strong Oxygen A absorption band around 765 nm is clearly visible in the intensity spectrum (top plot), whereas it has no impact on the normalized modulation pattern (bottom plot). The grey vertical bands indicate the wavelength bins that have been used for retrieving the aerosol parameters, matching the spectral bands of the co-located AERONET sun photometer, viz. 441, 675 and 870 nm, all with a full width at half maximum of 10 nm.
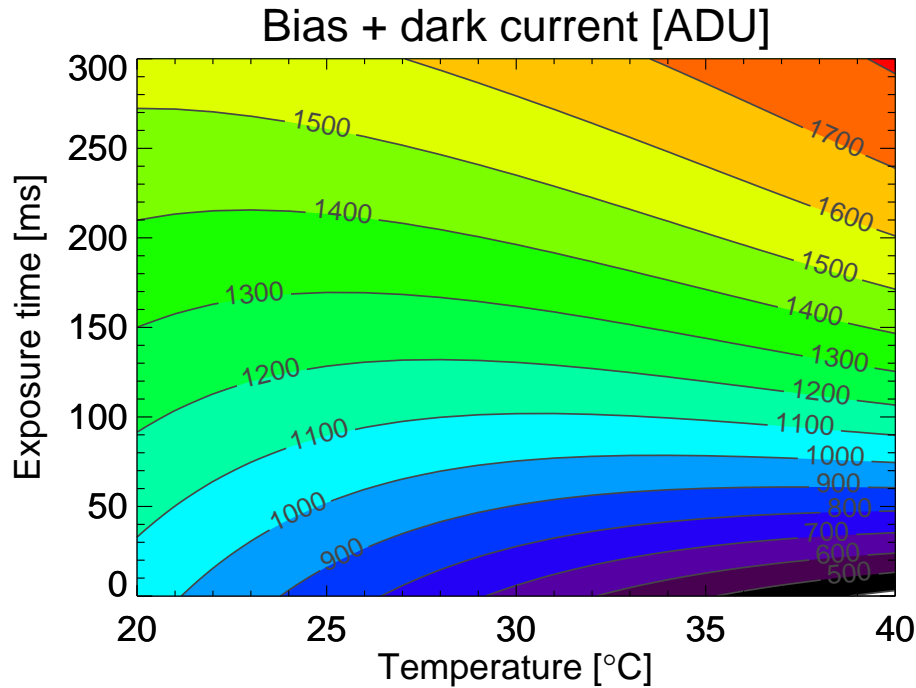
Figure 2. Calibration model of bias and dark current as a function of exposure time and temperature. The variable exposure time and direct exposure to weather results in a dark range of about 1000 ADU (out of a maximum of 65 536).
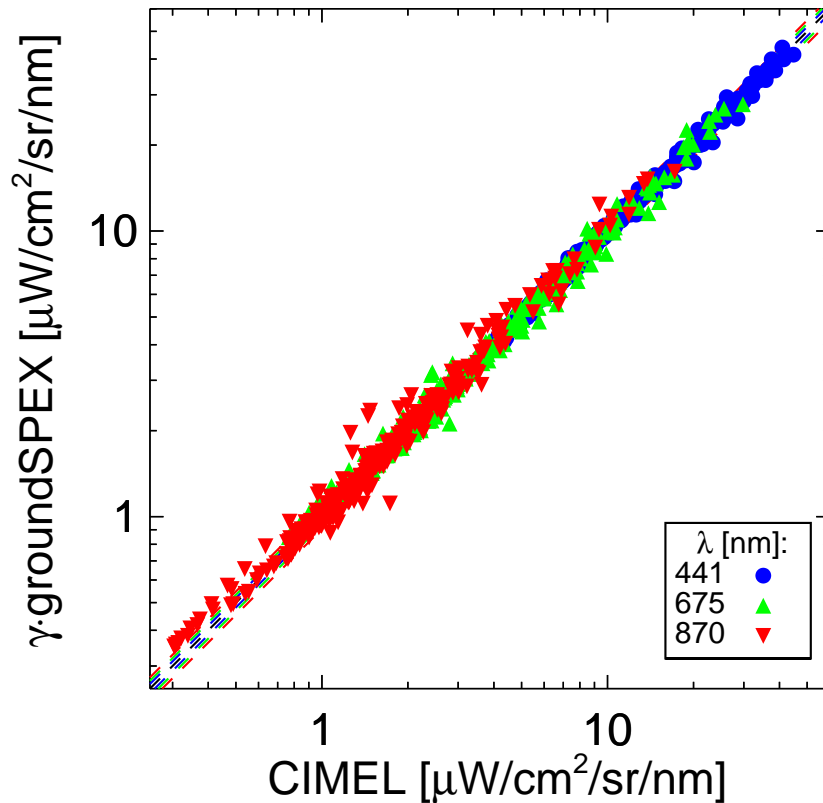
Figure 3. Correlation between sky radiances measured with groundSPEX and the CIMEL sun photometer used for the calibration of the gain $\gamma(\lambda)$ of groundSPEX. The dashed lines indicate the combined systematic and random error bars. Note the double logarithmic scale, so the errors scale with intensity.
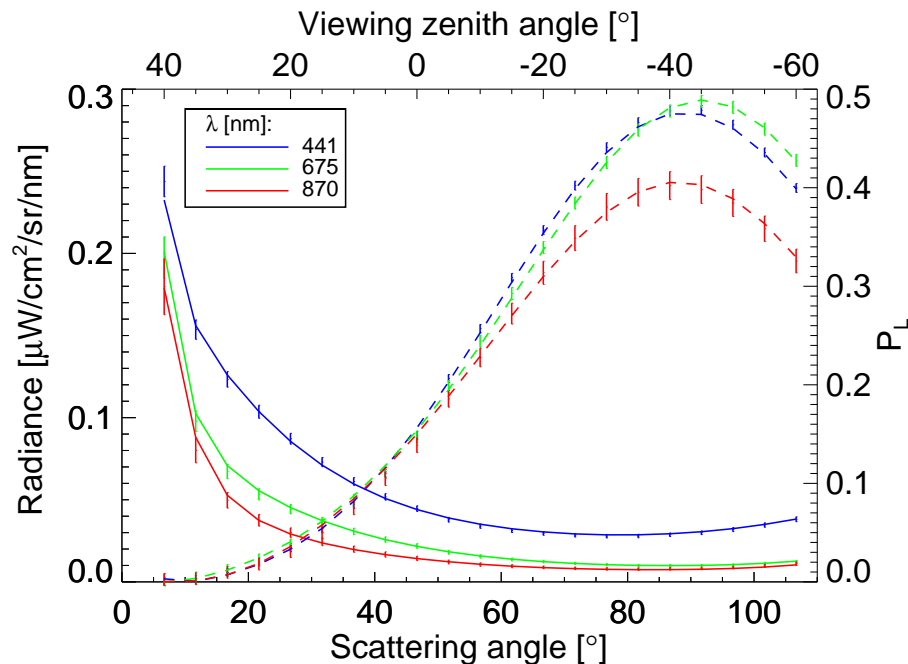
Title Page

Abstract | Introduction

Conclusions | References

Tables | Figures

|◄ | ►|

◄ | ►

Back | Close

Full Screen / Esc

Printer-friendly Version

Interactive Discussion

Figure 4. Measurements (displayed as vertical error bars) and retrieval algorithm best fit of spectral radiance (solid curves) and degree of linear polarization (dashed curves) as a function of scattering angle in the principal plane. The mean solar zenith angle was 46.66°, with a drift of $< 0.03°$ during the measurements. CESAR Observatory, 9 July 2013, 14:55 UTC.

Figure 5. Aerosol optical thickness at 550 nm during the day of 9 July 2013, at Cabauw, the Netherlands. GroundSPEX diffuse sky measurements are compared with AERONET direct sun measurements. The red data point at 14:55 UTC is retrieved from the measurements displayed in Fig. 4.
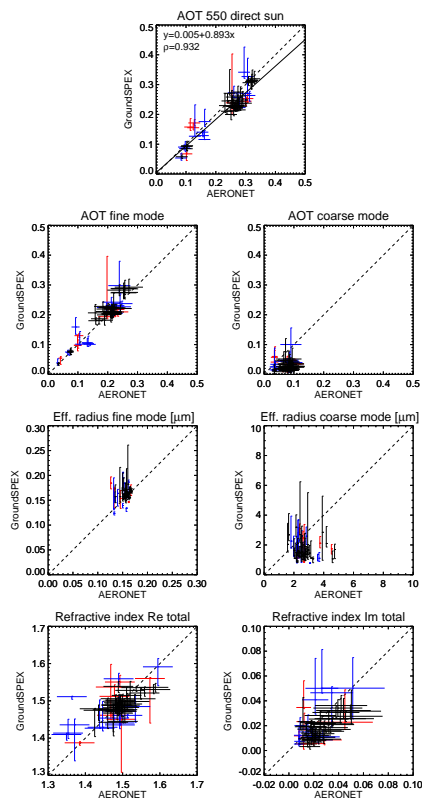
Figure 6. Aerosol parameters retrieved with the groundSPEX instrument, compared to AERONET. The different colors correspond to different goodness-of-fit values of the retrieval: $5 \leq \chi^2 \leq 10$ (red), $2 \leq \chi^2 \leq 5$ (blue), $\chi^2 \leq 2$ (black). The dashed lines indicate the ground-SPEX = AERONET scenario. The measurements were performed on 7, 8 and 9 July and 5 September 2013, at Cabauw, the Netherlands.